Front. Chem. Sci. Eng. 2024, 18(11): 133
https://doi.org/10.1007/s11705-024-2480-7

RESEARCH ARTICLE

Formulation of zeolite-mesoporous silica composite catalysts for light olefin production from catalytic cracking

Hassan Alhassawi (✉)[1], Edidiong Asuquo[1], Shima Zainal[1], Yuxin Zhang[1], Abdullah Alhelali[1], Zhipeng Qie[1,2], Christopher M. A. Parlett[1,3,4,5], Carmine D’Agostino[1], Xiaolei Fan[1], Arthur A. Garforth (✉)[1]

1 Department of Chemical Engineering, School of Engineering, The University of Manchester, Manchester M13 9PL, UK
2 Faculty of Environment and Life, Beijing University of Technology, Beijing 100124, China
3 Diamond Light Source Harwell Science and Innovation Campus, Oxfordshire OX11 0DE, UK
4 University of Manchester at Harwell, Diamond Light Source Harwell Science and Innovation Campus, Oxfordshire OX11 0DE, UK
5 UK Catalysis Hub, Research Complex at Harwell, Rutherford Appleton Laboratory, Oxfordshire OX11 0FA, UK

Abstract Framework materials such as zeolites and mesoporous silicas are commonly used for many applications, especially catalysis and separation. Here zeolite-mesoporous silica composite catalysts (employing zeolite Y, ZSM-5, KIT-6, SBA-15 and MCM-41 mesoporous silica) were prepared (with different weight percent of zeolite Y and ZSM-5) and assessed for catalytic cracking (using *n*-heptane, as the model compound at 550 °C) with the aim to improve the selectivity/yield of light olefins of ethylene and propylene from *n*-heptane. Physicochemical properties of the parent zeolites and the prepared composites were characterized comprehensively using several techniques including X-ray diffraction, nitrogen physisorption, scanning electron microscopy, fourier transform infrared spectroscopy, pulsed-field gradient nuclear magnetic resonance and thermogravimetric analysis. Catalytic cracking results showed that the ZY/ZSM-5/KIT-6 composite (20:20:60 wt %) achieved a high *n*-heptane conversion of 85% with approximately 6% selectivity to ethylene/propylene. In contrast, the ZY/ZSM-5/SBA-15 composite achieved a higher conversion of 95% and an ethylene/propylene ratio of 8%, indicating a more efficient process in terms of both conversion and selectivity. Magnetic resonance relaxation analysis of the ZY/ZSM-5/KIT-6 (20:20:60) catalyst confirmed a micro-mesoporous environment that influences *n*-heptane diffusion and mass transfer. As zeolite Y and ZSM-5 have micropores, *n*-heptane can move and undergo hydrogen transfer reactions, whereas KIT-6 has mesopores that facilitate *n*-heptane’s accessibility to the active sites of zeolite Y and ZSM-5.

Keywords zeolites, mesoporous silica, composite catalysts, catalytic cracking, light olefins

1 Introduction

Light olefins (LOs, including ethylene ($C_2 =$), propylene ($C_3 =$), and butylene ($C_4 =$)) are important platform chemicals for producing cosmetics, lubricants, rubbers, detergents and polymers [1], and the current demand for LOs is predicted to reach $329.30 billion by 2028, growing at a rate of 4.5% from 2020 [2,3]. However, the supply of LOs is limited by traditional production routes such as steam cracking. Therefore, enhancing the production of LOs via optimising traditional technologies (such as catalytic cracking) is regarded as the alternative to meet the high market demand of LOs globally. One of the conventional technologies to produce LOs worldwide is the fluidized catalytic cracking (FCC) process using naphtha which allows for 22% of global LOs production [4]. Yet, the development of LOs-selective FCC catalysts is needed to increase the FCC capacity for LOs production.

Zeolites, especially Zeolite Y (ZY) and ZSM-5, are key components in FCC particles since 1960 [5], whose formulation is based on several components including zeolites, clay, binder and filler. In the matrix in FCC particles ZY is employed to increase liquefied petroleum gas, olefins, and gasoline by primary cracking of heavy liquid paraffin through the 12 membered rings (MR) in its large-pore framework. Comparatively, addition of ZSM-5 is recognized to be able to increase the yield of LOs because its medium 10 MR pore size favors the monomolecular mechanism to promote the selectivity to

Received January 20, 2024; accepted April 20, 2024; online July 20, 2024

E-mails: hassan.alhassawi@postgrad.manchester.ac.uk (Alhassawi H), arthur.garforth@manchester.ac.uk (Garforth A A)

LOs [6].

Zeolites have microporous frameworks, providing the essential acid active sites and shape selectivity needed for high performance in hydrocarbon cracking reactions [7]. However, the micropores can impose diffusion limitation for bulky reactants, reducing catalytic effectiveness and causing deactivation [8]. To address this issue, strategies focusing on engineering hierarchical meso-micro-porous zeolites and/or composites were developed, exemplified by hierarchical ZY by different post-synthetic treatments (such as chemical treatment using chelating agents [9]) and ZSM-5/MCM-41 composite [10]. Another possible strategy is physically mixing microporous zeolites with mesoporous silicas, such as KIT-6, MCM-41, and SBA-15, to prepare the composite catalysts, in which the presence of mesoporous silicas in the FCC particles can enhance the mass transfer within the FCC particles and/or pre-crack the reactant molecules, then zeolites can do the further cracking with the improved selectivity. The latter approach is flexible allowing independent tuning of the properties of each component to optimize the activity/selectivity of the resulting composite catalyst.

Here, we explore the effect of composite catalyst formulation on the performance of catalytic cracking with the aim of improving the production of LOs of $C_2 =$, $C_3 =$, and $C_4 =$. The composites catalysts were formulated using two zeolites (of ZY and ZSM-5) and three ordered mesoporous silicas (of KIT-6, SBA-15, and MCM-41) by varying the weight percent of the zeolites and maintaining the weight percent of silicas at 60 wt %. The prepared composite catalysts were characterized comparatively using various techniques to understand their physicochemical properties and assessed using catalytic cracking of *n*-heptane (*n*-C_7) (as the model compound of naphtha). In addition, a pulsed-field gradient nuclear magnetic resonance (PFG-NMR) study of the selected composite catalysts was conducted to know the molecular diffusion properties, which was correlated with the catalytic performance.

2 Experimental

2.1 Materials and Chemicals

ZSM-5 (CBV 2314) and ZY (CBV 712) zeolites, both in NH_3 form (with the silicon to aluminum ratio (Si/Al) of 11.5 and 6, respectively) were purchased from Zeolyst International, and the mesoporous MCM-41 was purchased from ACS Materials. The zeolites were first calcined at 550 °C for 5 h, heating from ambient at 2 $°C\cdot min^{-1}$, to convert to the H-form counterparts. HCl (12 $mol\cdot L^{-1}$), tetraethoxysilane (TEOS, 99%) and *n*-butanol (*n*-BuOH, 99.5%) were purchased from Fisher Scientific. Poly (ethylene glycol)-block-poly (propylene glycol)-block-poly (ethylene glycol) PEO_{20}-PPO_{70}-PEO_{20} (P123 with MW = 5800, Aldrich) was used as the direct-structuring agent for synthesizing the mesoporous silicas of SBA-15 and KIT-6.

2.2 Synthesis of mesoporous SBA-15 and KIT-6 silica

Mesoporous SBA-15 was synthesized using the procedure reported elsewhere [11]. In detail, 10 g of P123 was dissolved in the HCl solution (containing 74.5 mL of deionized water and 291.5 mL of 12 $mol\cdot L^{-1}$ HCl) under stirring (at 300 $r\cdot min^{-1}$) at 35 °C for 15 min (the temperature was maintained by an oil bath). Then, 20 mL of TEOS was added dropwise for 5 min under 300 $r\cdot min^{-1}$ at 35 °C to form a homogeneous liquid, and the mixture was stirred continuously at 35 °C and 300 $r\cdot min^{-1}$ for 20 h in the sealed flask. The resulting mixture was transferred to a sealed 1000 mL round-bottomed flask with a condenser attached and placed in an oil bath for 24 h at 80 °C under static conditions. After the synthesis, the solid product was filtered and dried at 80 °C for 12 h without washing, followed by calcination at 500 °C for 6 h (ramp rate = 1 $°C\cdot min^{-1}$).

Mesoporous KIT-6 was prepared following the procedure reported in the literature [12,13]. The synthesis first involves dissolving the surfactant P123 (~10 g) in the *n*-BuOH-HCl mixture containing 366 mL of deionized water, 12.3 mL of *n*-BuOH and 16.3 mL of 12 $mol\cdot L^{-1}$ HCl in a polypropylene bottle. The mixture was stirred at 300 $r\cdot min^{-1}$ and kept at 35 °C for 15 min. Then TEOS (20.0 mL) was added dropwise for 5 min under 300 $r\cdot min^{-1}$ at 35 °C to form a homogeneous liquid, and the mixture was stirred continuously at 300 $r\cdot min^{-1}$ for 20 h at 35 °C in a sealed 500 mL flask that was placed in an oil bath. The resulting suspension was transferred to a sealed 1000 mL round-bottomed flask (same as above in the synthesis of SBA-15) for static hydrothermal synthesis for 24 h at 80 °C. Finally, the resulting solid product was filtered, and dried at 80 °C for 12 h without washing, followed by calcination at 500 °C for 6 h (ramp rate = 1 $°C\cdot min^{-1}$).

2.3 Formulation of the composite catalysts

The physical mixtures of ZY/ZSM-5/X, where X = KIT-6, SBA-15 or MCM-41, were prepared by stirring the three components in deionized water for 3 h at ambient temperature. The weight percent of the components are detailed in Table 1, and the ratio of deionized water to the mixture was 1.5:1 w/w. After the 3 h mixing, the resulting slurry was dried in an oven at 120 °C overnight, then the resulting dry solid was calcined at 550 °C for 6 h (ramp rate = 2 $°C\cdot min^{-1}$). Finally, the composites were pelletized (with the particle sizes of 100 to 450 μm).

Table 1 Proportion of components in the formulated composite catalysts

Composite catalyst	Weight percent of the component/wt %		
	ZY	ZSM-5	Mesoporous silica
ZY/ZSM-5/KIT-6(35:5:60)	35	5	60
ZY/ZSM-5/KIT-6(30:10:60)	30	10	60
ZY/ZSM-5KIT-6(20:20:60)	20	20	60
ZY/ZSM-5/SBA-15(35:5:60)	35	5	60
ZY/ZSM-5/SBA-15(30:10:60)	30	10	60
ZY/ZSM-5/SBA-15(20:20:60)	20	20	60
ZY/ZSM-5/MCM-41(35:5:60)	35	5	60
ZY/ZSM-5/MCM-41(30:10:60)	30	10	60
ZY/ZSM-5/MCM-41(20:20:60)	20	20	60

2.4 Characterization of materials

Powder X-ray diffraction (PXRD) of the composite catalysts was carried out using a portable desktop XRD instrument (D2 PHASER, Bruker) with Cu kα radiation (λ = 1.5406 Å) at 30 mA and 40 kV. The samples were scanned with a 2θ interval of 5° to 90°, a step size of 0.02° and a step time of 8 s. Low-angle PXRD was performed using a D8 ADVANCE diffractometer (Bruker) instrument using a Cr Ka radiation (λ = 1.5406 Å) at 30 mA and 40 kV. The samples were scanned with a 2θ interval of 0.5° to 5°, a step size of 0.02° and a step time of 8 s. An energy-dispersive X-ray fluorescence (EDXRF) spectrometer was conducted using the PANalytical MiniPal 4 EDXRF instrument for elemental composition analysis operating at 30 kV to calculate the bulk Si/Al ratio of materials. N_2 adsorption and desorption isotherms of materials were measured using a Micromeritics ASAP 2060 physisorption analyzer. The sample (about 150 mg) was degassed at 300 °C under a vacuum (0.5 mmHg) for 4 h before the physisorption analysis at the liquid nitrogen temperature of –196 °C (77 K). The specific surface area of the materials was determined using the Brunauer-Emmett-Teller (BET) method, and the pore size distribution (PSD) was estimated by the Barrett-Joyner-Halenda (BJH) method based on the desorption isotherm. Fourier-transform infrared spectroscopy (FTIR) was carried out using a Bruker Vertex 7.0 spectrometer. The spectra were collected with a spectral resolution of 4 cm^{-1}, 32 scans, and over a wavenumber range of 4000–400 cm^{-1}. Scanning electron microscopy (SEM) of the morphology of the composite catalysts was conducted using Tescan Vega 3 at 20 kV and under high vacuum pressure (10^{-6} to 10^{-7} torr). The working distance was 10–15 mm. Transmission electron microscopy (TEM) was conducted using an FEI Tecnai G2 20 microscope operated at an accelerating voltage of 200 kV and equipped with an Oxford Instruments X-Max TLE 80 EDX detector and a Gatan Orius CCD camera. Coke deposition on the used catalyst after the catalytic experiments was assessed by thermogravimetric analysis (TGA, Q600 TGA-DSC, TA Instruments). The temperature program and gas atmosphere were (i) under N_2 at 40 $cm^3 \cdot min^{-1}$ from room temperature to 650 °C, isothermally held for 60 min at 200 °C, 400 °C, and 650 °C, respectively, (ii) at 650 °C switching to air at 40 $cm^3 \cdot min^{-1}$ for 3 h.

2.5 PFG-NMR analysis

To study the diffusion of n-C_7 in the composite catalysts, PFG-NMR measurements were performed. In detail, the dried catalyst sample (~100 mg, dried at 120 °C for 3 h) saturated using n-C_7 for 48 h according to the reported procedure [14]. To remove the excess liquid from the sample, the saturated catalyst was gently dried using the filter paper. Then the catalyst was transferred to an NMR tube (of 5 mm diameter) to a depth of 25 mm, to fit a similar height of the radiofrequency coil in the probe of the spectrometer. The tube was sealed with polytetrafluoroethylene tape and left for 1 h to achieve thermal equilibrium before the measurement. PFG-NMR measurements were conducted at a higher magnetic field strength employing a Bruker spectrometer at 500 MHz with a diffusion probe to measure the relaxation times of T_1 and T_2 of the probe molecules in the sample. Measurements were conducted at ambient temperature (20 °C), employing stimulated echo using bipolar gradient pulse pair sequences for diffusion measurements, a 15 μs ^1H 90° pulse, a 1.4 ms sinusoidal gradient pulse width (δ), varying gradient pulse amplitudes ranging from 2% to 15% of 15 Tm^{-1} across 16 increments at diffusion intervals (Δ) of 100 ms.

2.6 Catalytic cracking

Catalytic cracking using different catalysts was performed using a fixed bed reactor. The reactor is a stainless-steel tube (inner diameter of 9 mm and outer diameter of 14 mm) packed with ~0.6 g catalyst (pelletized, 100–450 μm), and quartz wool and glass beads were used to support the catalyst bed. The catalyst was activated *in situ* by purged with air (50 $mL \cdot min^{-1}$) and heating the reactor to 550 °C at 10 $°C \cdot min^{-1}$ for 30 min, followed by N_2 (70 $mL \cdot min^{-1}$), at atmospheric pressure for 1 h. n-C_7 was then introduced to the reactor using N_2 as the carrier gas (passing through three bubblers in series in a chiller at –2 °C) to initiate the reaction. The schematic of the experimental rig is shown in Fig. 1. The cracking reactions were typically conducted for 4 h at atmospheric pressure with a weight hourly space velocity (WHSV) of 0.41 h^{-1}, and the stability test was conducted for 12 h.

Gas samples from the outlet of the reactor were taken every hour for gas chromatography (GC) analysis using a Varian 3800 GC equipped with a Restek PLOT Al_2O_3 KCl capillary column (50 m × 5 mm × 0.32 μm) and a flame ionization detector. The temperature program of the oven is: isothermal at 70 °C for 5 min, ramp to 225 °C at 10 $°C\cdot min^{-1}$ then isothermal at 225 °C for 30 min. The GC was calibrated using a standard gas mixture with a concentration of 1% mol of C_1–C_5 (BOC Linde Group). Based on the peak area from a GC chromatogram, the conversion (C_{n-C_7}), selectivity ($S_{C_xH_y}$), and yield ($Y_{C_xH_y}$) were calculated using Eqs. (1–3).

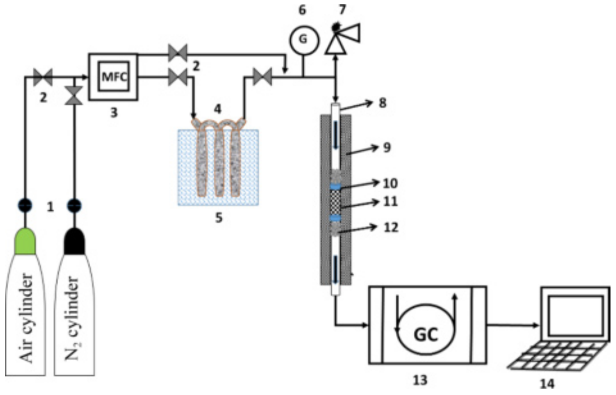

Fig. 1 Schematic of the experimental rig for performing the catalytic cracking reaction. 1. pressure regulators for N_2 and air; 2. valves; 3. mass flow controllers; 4. bubblers; 5. chiller bath; 6. pressure gauge; 7. pressure relief valve; 8. reactor tube; 9. furnace; 10. glass wool; 11. catalyst bed; 12. glass beads; 13. GC; 14. data collector.

$$C_{n\text{-}C_7}(\%) = \frac{n\text{-}C_{7(\mathrm{in})} - n\text{-}C_{7(\mathrm{out})}}{n\text{-}C_{7(\mathrm{in})}} \times 100\%, \tag{1}$$

$$S_{C_xH_y}(\%) = \frac{C_xH_y}{n\text{-}C_{7(\mathrm{in})} - n\text{-}C_{7(\mathrm{out})}} \times 100\%, \tag{2}$$

$$Y_{C_xH_y}(\%) = S_{C_xH_y} \times C_{n\text{-}C_7}, \tag{3}$$

where $n\text{-}C_{7(\mathrm{in})}$ and $n\text{-}C_{7(\mathrm{out})}$ are the mole of $n\text{-}C_7$ in the inlet and outlet stream of the reactor, respectively, C_xH_y is the total mole of LOs ($C_2=$, $C_3=$, and $C_4=$) produced.

3 Results and discussion

3.1 Physicochemical properties of the materials under investigation

Small-angle X-ray patterns of the commercial MCM-41 and the as-prepared SBA-15 and KIT-6 mesoporous silicas (Fig. 2(a)) confirm their well-ordered frameworks with uniform mesopores as evidenced by the relevant characteristic diffraction peaks. In details, for MCM-41, the peaks at 2θ = 2.3° (100), 3.8° (110), and 4.4° (200) reflections, corresponding to the reflections of the 2D hexagonal (space group p6mm) symmetry [15]. The

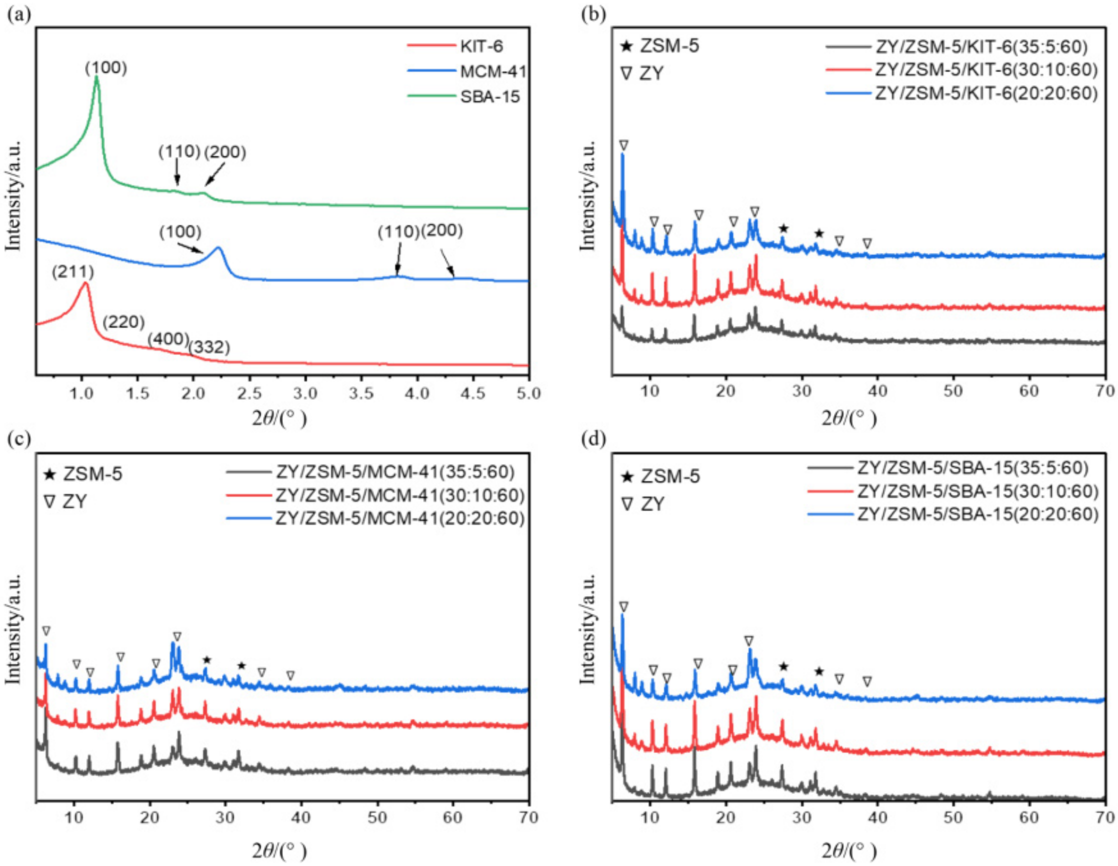

Fig. 2 (a) Small-angle XRD patterns of the mesoporous silicas; wide-angle XRD diffraction patterns of (b) ZY/ZSM-5/KIT-6 group; (c) ZY/ZSM-5/MCM-41 group, and (d) ZY/ZSM-5/SBA-15.

diffraction pattern of SBA-15 shows the typical reflections in the 2θ range of < 5° with the major peak at about 1.1° (corresponding to the (100) plane) and two insignificant humps at 2θ about 1.8°, and 2.2° (corresponding to the (110) and (220) planes, respectively) [16,17], confirming the hexagonal ordered structure. The low-angle diffraction pattern for KIT-6 shows the distinct peak at 2θ of 1.05°, being assigned to the (211) plane [18], while other relevant diffraction peaks assignable to the (220), (400), and (332) planes are not well resolved.

Figures 2(b) and 2(c) show the wide-angle XRD patterns of the formulated composite catalysts, in which the characteristic diffraction peaks of the ZSM-5 MFI crystal structure (indicated by the star symbols) and that of the ZY FAU crystal structure (indicated by the nabla symbols), respectively) can be identified clearly. The results suggest that after the formulation synthesis the frameworks of ZY and ZSM-5 remained intact. In additional, the amorphous humps at around 2θ of 20°–30° were identified in the composites, confirming the presence of KIT-6, SBA-15, and MCM-41 in them [19]. Interestingly, the diffraction peak intensities of ZY and ZSM-5 do not correspond to the variation in their weight percent in the composite catalysts, which could be attributed to the heterogeneous distribution of the components in the samples used for XRD characterization.

The textural properties of the mesoporous silicas and composite catalysts were examined by N_2 physisorption, as shown in Fig. S1 (cf. Electronic Supplementary Material, ESM) and Table 2. N_2 adsorption-desorption isotherms and BJH PSDs of the mesoporous silicas (KIT-6, MCM-41, and SBA-15) are shown in Fig. S1, displaying the typical IV isotherms with hysteresis loops, which proves the presence of uniform mesopores with narrow PSD. MCM-41 shows a narrow PSD centring at about 1.6 nm, the KIT-6 synthesized in this study shown a larger mesopore size of about 2.4 nm. Regarding the synthesized SBA-15, its PSD is widest ranging from 2 to 4 nm. All three mesoporous silicas show the high specific external surface areas (S_{ext}) and mesopore volumes (V_{meso}). After the formulation with different proportions of ZY and ZSM-5 (Fig. S2, cf. ESM), the total specific external surface areas (S_{BET}) and mesopore volumes of the resulting composites decreased by 10%–20%, while the micropore surface areas (S_{micro}) and micropore volumes (V_{micro}) were enhanced by 50%–55%, confirming the improved microporosity provided by the zeolites. The findings demonstrate that the formulated composites consist of both well-developed mesoporous and microporous properties, which could potentially benefit their performance in catalysis, outperforming the individual materials

The N_2 physisorption isotherms of the formulated composites are shown in Fig. S2, and that of the three selected samples is shown in Fig. 3. The Type IV isotherms (Fig. 3(a)) suggest the overall mesoporous structure since the main components in them are mesoporous silica. The BJH PSDs (Fig. 3(b)) show that the ZY/ZSM-5/KIT-6 (20:20:60) and ZY/ZSM-5/SBA-15 (20:20:60) composites possess similar pore sizes centered at about 2.4 nm, while that for ZY/ZSM-5/MCM-41 (20:20:60) is narrower centered at about 1.6 nm. The results suggest that these composite catalysts contain the mixed mesoporosity and microporosity, potentially benefiting the accessibility of the active sites (in zeolites) to reactant molecules and mass transport within them. For the same category composites, the PSDs (Fig. S2) are similar without being affected significantly by the variation in the weight percent of the two zeolites.

The SEM micrographs (Fig. S3, cf. ESM) illustrate the morphology and microstructure of the selected composite catalysts of ZY/ZSM-5/KIT-6 (20:20:60), ZY/ZSM-5/SBA-15 (20:20:60), and ZY/ZSM-5/MCM-41 (20:20:60). Figure S3(a) shows the heterogenous distribution of ZY, ZSM-5, and KIT-6 particles in ZY/ZSM-5/KIT-6 (20:20:60), and the large irregular-shaped crystals of

Table 2 Textural properties of the mesoporous silicas and the composite catalysts

Materials	Specific surface area[a)]/($m^2 \cdot g^{-1}$)			Specific surface area[b)]/($cm^3 \cdot g^{-1}$)			Si/Al[c)]
	S_{BET}[a)]	S_{ext}[b)]	S_{micro}[c)]	V_{total}[d)]	V_{micro}[e)]	V_{meso}[f)]	
KIT-6	755	559	202	0.34	0.11	0.23	–
MCM-41	810	767	42	0.33	0.02	0.31	–
SBA-15	755	442	312	0.66	0.16	0.5	–
ZY/ZSM-5/KIT-6(35:5:60)	601	418	183	0.30	0.1	0.2	48.4
ZY/ZSM-5/KIT-6(30:10:60)	585	351	234	0.27	0.12	0.15	47.5
ZY/ZSM-5/KIT-6(20:20:60)	541	331	211	0.25	0.11	0.14	42.1
ZY/ZSM-5/MCM-41(35:5:60)	726	564	161	0.31	0.08	0.23	36.7
ZY/ZSM-5/MCM-41(30:10:60)	705	535	169	0.31	0.09	0.22	36.2
ZY/ZSM-5/MCM-41(20:20:60)	718	583	135	0.31	0.07	0.24	36.3
ZY/ZSM-5/SBA-15(35:5:60)	604	391	212	0.30	0.11	0.19	16
ZY/ZSM-5/SBA-15(30:10:60)	535	301	234	0.25	0.12	0.13	20.4
ZY/ZSM-5/SBA-15(20:20:60)	577	368	210	0.30	0.11	0.19	26.7

a) Total surface area (S_{BET}) by the BET method, external surface area (S_{ext}) = $S_{BET} - S_{micro}$, microspore surface area by the *t*-plot method; b) total pore volume at P/P_0 (V_{total}) = maximum pore volume, microspores volume (V_{micro}), mesoporous volume (V_{meso}); c) by XRF; d) by the BJH method.

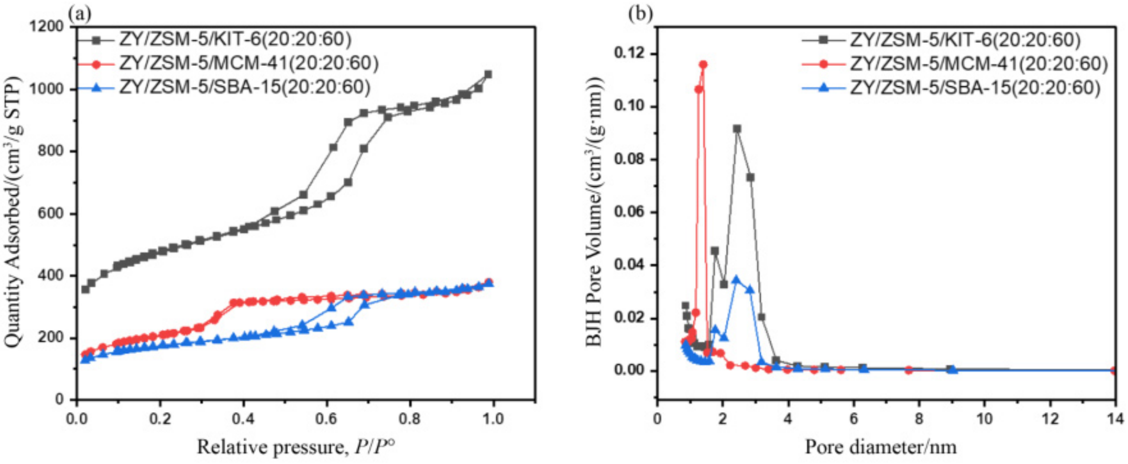

Fig. 3 (a) N_2 adsorption-desorption isotherms of ZY/ZSM-5/KIT-6(20:20:60), ZY/ZSM-5/MCM-41(20:20:60), and ZY/ZSM-5/SBA-15(20:20:60), and (b) the associated PSD by the BJH method.

KIT-6 with rough terraces could be identified [20]. Similar heterogenous microstructures were found for the ZY/ZSM-5/SBA-15 (20:20:60) and ZY/ZSM-5/MCM-41 (20:20:60) composites as well (Figs. S3(b) and S3(c)), with the former having the presence of short-rod particles (for SBA-15 [17]) and the latter having the spherical particles smaller than 0.5 μm (for MCM-41 [21]). For the ZY/ZSM-5 crystals, they cannot be identified clearly in the composite catalysts by SEM. TEM characterization of the composite catalysts was conducted. As shown in Fig. 4(a), the parallel mesoporous channels of KIT-6 [22] can be clearly seen in ZY/ZSM-5/KIT-6 (20:20:60). In Fig. 4(b), the overlapped phases of SBA-15 mesoporous silica and ZSM-5 zeolite were found in ZY/ZSM-5/SBA-15 (20:20:60). The amorphous SBA-15 is visible next to the crystalline ZSM-5 phase. However, the ordered mesoporous structure of SBA-15 is less clear. Like ZY/ZSM-5/SBA-15 (20:20:60), similar microscopic structures were found as well in ZY/ZSM-5/MCM-41 (20:20:60), showing the presence of both crystalline zeolite phases and amorphous MCM-41 phase (Fig. 4(c)).

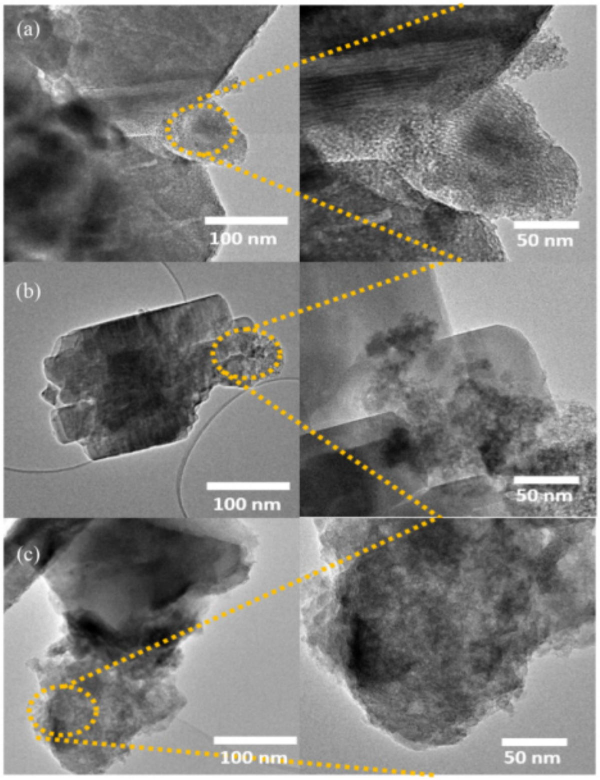

Fig. 4 TEM images of the selected composite catalysts: (a) ZY/ZSM-5/KIT-6 (20:20:60); (b) ZY/ZSM-5/SBA-15 (20:20:60), and (c) ZY/ZSM-5/MCM-41 (20:20:60).

FTIR spectra of the zeolites and mesoporous silicas are shown in Fig. S4(a) (cf. ESM). All mesoporous silicas show the characteristic vibration bands of Si–O–Si, including the asymmetric, symmetric stretching vibrations, bending vibrations at ~1064 cm^{-1} [23], ~795 cm^{-1} [22], and ~434 cm^{-1} [24], respectively. For zeolites, it shows two bands, which are related to the external linkage banding vibration of Al–O_4 tetrahedra at ~608 cm^{-1} [25] and ~529 cm^{-1} [26,27], depending on the type of zeolite frameworks (i.e., FAU or MFI). The IR bands at ~1243 cm^{-1}, ~811 cm^{-1}, and ~608 cm^{-1} [26,28], are associated with the internal linkage symmetric stretching and asymmetrical stretching in the zeolite framework, respectively. The IR spectra of the formulated composites are shown in Figs. S4(b–d). The composites show a decrease in the intensity of the characteristic framework bands, indicating the possible interaction between the mesoporous silicas and the zeolites. The decrease in the intensity of the bands related to the zeolitic frameworks (of ~612 cm^{-1}–466 cm^{-1} and ~1383 cm^{-1}–810 cm^{-1}) in the composites could be due to the dilution by the mesoporous silica (with the weight percents of 60%). In addition, the significant presence of OH stretching bands (e.g., the band at about 3410 cm^{-1}) suggests the water adsorption in the composites after formulation.

3.2 Catalytic cracking of *n*-Hptane (*n*-C_7)

Catalytic cracking of *n*-C_7 was first performed using the pristine zeolites and mesoporous silicas, and the conversion results as a function of time-on-stream (ToS) are shown in Fig. S5(a) (cf. ESM). Mesoporous silicas are not capable of cracking *n*-C_7, showing comparable insignificant *n*-C_7 conversions (about 2%). Conversely, over the two zeolites the initial *n*-C_7 conversions were considerable at about 95%. The ZSM-5 zeolite (Si/Al = 11.5) was very stable with only 5% loss in activity over 4 h on stream. Comparatively, the ZY zeolite (Si/Al = 6) deactivated continuously with the final *n*-C_7 conversion at 71%. This could be due to the low Si/Al of ZY which contributed to coking during catalytic cracking.

Figure S5(b) shows the total yield of LOs from the system employing different frameworks. Again, the mesoporous silicas showed insignificant yields of LOs. ZY presents an initial higher total LOs yield of 41%, which decreased gradually to about 22% after 4 h on stream. Conversely, ZSM-5 shows a very stable total LOs yield over the catalytic assessment (at about 22.6%). Detailed distributions of the selectivity to different LOs are shown in Fig. S6 (cf. ESM). In detail, ZY shows the initial higher selectivity to C_2 = and C_3 = , which gradually decreased to about 4.5% and 20%, respectively, while the selectivity of ZY to C_4 = was rather stable (at about 6.7%, Fig. S6(a)). Overall, ZY was selective to C_3 = and C_4 = due to its intrinsic large 12-MR pores [29], which allows heavier hydrocarbons to accumulate, causing the catalyst's deactivation [30]. Conversely, ZSM-5 was more selective to C_2 = (at about 13.5%), followed by C_3 = (at about 9%), and produced rather insignificant C_4 = , as shown in Fig. S6(b). ZSM-5 can constrain the transition state and increase C_2 = and C_3 = olefin production due to its three-dimensional pore network and 5.4–5.6 nm ring openings [31]. In addition, compared to the ZY, ZSM-5 was more stable due to the smaller pore sizes and less acidic nature [32]. Under the same condition, catalytic cracking of *n*-C_7 over different composites was conducted comparatively, and the results are shown in Fig. 5.

It is worth noting that, for a specific silica, variation in the formulation of zeolites caused the significant effect on the catalyst activity of the composite catalysts. Taking the ZY/ZSM-5/KIT-6 composites as the example, an increase in the weight percent of ZSM-5 from 5% to 20% leads to the significant increase in *n*-C_7 conversion, that is, ~35.4% for ZY/ZSM-5/KIT-6 (35:5:60) vs ~82.4% for ZY/ZSM-5/KIT-6 (20:20:60), as well as the total selectivity to LOs, i.e., from ~15.8% to ~27%. Interestingly, similar trends were measured for the other two sets of composite catalysts based on SBA-15 and MCM-41, i.e., the composites with 20 wt % ZSM-5 showed the best catalytic cracking performance. The findings demonstrate the important role played by the ZSM-5 zeolite on the activity of the composite catalysts.

By comparing the catalytic performance of the composites with a fixed formulation of zeolites, the effect of the mesoporous silicas on the catalysis was identified. For the composites with 35 wt % ZY and 5 wt % ZSM-5, the steady-state *n*-C_7 conversion follows the order of ZY/ZSM-5/MCM-41(35:5:60) > ZY/ZSM-5/SBA-15 (35:5:60) > ZY/ZSM-5/KIT-6 (35:5:60). For the composites with 30 wt % ZY and 10 wt % ZSM-5, ZY/ZSM-5/MCM-41 (30:10:60) again shows the highest *n*-C_7 conversion at about 83.4%, conversely, the ZY/ZSM-5/SBA-15 (30:10:60) composite achieved the lowest *n*-C_7 conversion at about 40%. The better performance of the composites containing 5% ZSM-5 and 10% ZSM-5 with MCM-41 is likely a result of the tight range of mesopores size and also the smaller size of the mesopores (typically 0.8–1.2 nm, cf. ESM). The ZSM-5 and the ZY crystals are typically aggregated between 5 to 2500 nm (typically 250–500 nm) and hence will most likely be coating the mesoporous silicas and not inside any pore structure. Therefore performance will be related to the morphology of the individual silicas (e.g., MCM-41, KIT-6, and

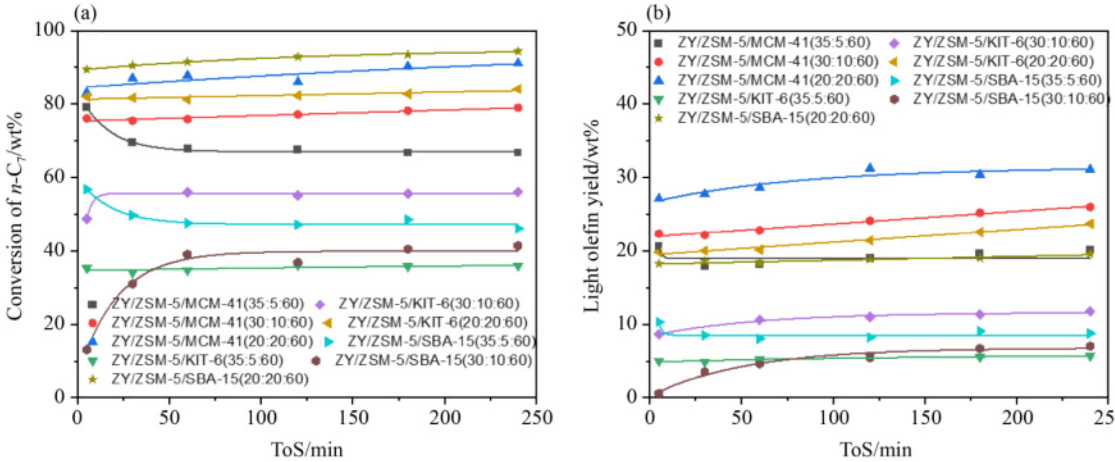

Fig. 5 (a) Conversions of *n*-C_7 and (b) total yields of LOs over different composite catalysts (conditions: t = 550 °C, WHSV = 0.4 h^{-1}, ToS = 4 h, P = atmospheric pressure).

SBA-15).

For the composites with the equal 20 wt % ZY and ZSM-5 formulation, ZY/ZSM-5/SBA-15 (20:20:60) showed that highest n-C_7 conversion at about 92% and total selectivity to LOs, as shown in Fig. 5. The addition of 20% ZSM-5 increased activity significantly and the overall conversion of all three composite catalysts was comparable (with conversions in the range 85% ± 5%) suggesting that the support has less influence compared to increase in ZSM-5 content.

The results shown here demonstrate the importance of balancing acidity (from zeolites) and mesopore space (from silicas) to optimize the catalytic cracking performance of the composites. Overall, ZY/ZSM-5/SBA-15 (20:20:60), ZY/ZSM-5/MCM-41 (20:20:60), and ZY/ZSM-5/KIT-6 (20:20:60) were identified as the top three best performed composite catalysts under investigation, which were further assessed.

Table 3 shows the detailed comparison of the catalytic performance of ZY/ZSM-5/KIT-6 (20:20:60), ZY/ZSM-5/SBA-15 (20:20:60), and ZY/ZSM-5/MCM-41 (20:20:60). ZY/ZSM-5/KIT-6 (20:20:60) and ZY/ZSM-5/SBA-15 (20:20:60) have the similar olefin-to-paraffin ratio (O/P) of about 0.7, while ZY/ZSM-5/MCM-41 (20:20:60) favors LO production based on its higher O/P ratio of 1.1. Among all the catalysts tested, the ZY/ZSM-5/SBA-15 (20:20:60) catalyst shows higher selectivity to LOs (26%). The hydrogen transfer coefficient (HTC) measures a catalyst's efficiency in facilitating hydrogen atom transfer between molecules, and the HTC of the three catalysts was comparable since the zeolite formulation in them was the same. Overall, results presented in Table 3 show that the details of product information of the systems employing ZY/ZSM-5/SBA-15 (20:20:60) and ZY/ZSM-5/KIT-6 (20:20:60) are similar, while that of the system over ZY/ZSM-5/MCM-41 (20:20:60) is slightly different.

Figure 6(a) shows the n-C_7 conversion from the stability tests of the three catalysts (as a function of ToS). Again, the ZY/ZSM-5/SBA-15 (20:20:60) composite

Table 3 Averaged activity and selectivity data of n-C_7 cracking over the selected composite catalysts at 550 °C, 0.4 h^{-1} and atmospheric pressure

Composite catalyst	Conversion	$C_{2=}$–$C_{4=}$ a)	$C_{2=}/C_{3=}$	$C_{2=}/C_2$	$C_{3=}/C_3$	$C_{4=}/C_4$	O/P b)	HTC c)
	%			–				
ZY/ZSM-5/SBA-15(20:20:60)	84	26.2	0.8	2.5	0.6	0.4	0.7	0.7
ZY/ZSM-5/KIT-6(20:20:60)	94	26.6	0.6	2.5	0.7	0.5	0.7	0.7
ZY/ZSM-5/MCM-41(20:20:60)	82	25.5	0.5	2.4	0.7	0.5	1.1	0.6

a) $C_{2=}$–$C_{4=}$: averaged total yield of LOs; b) O/P: olefin-to-paraffin ratio; c) HTC = (n-C_4 + i-C_4)/$C_{4=}$).

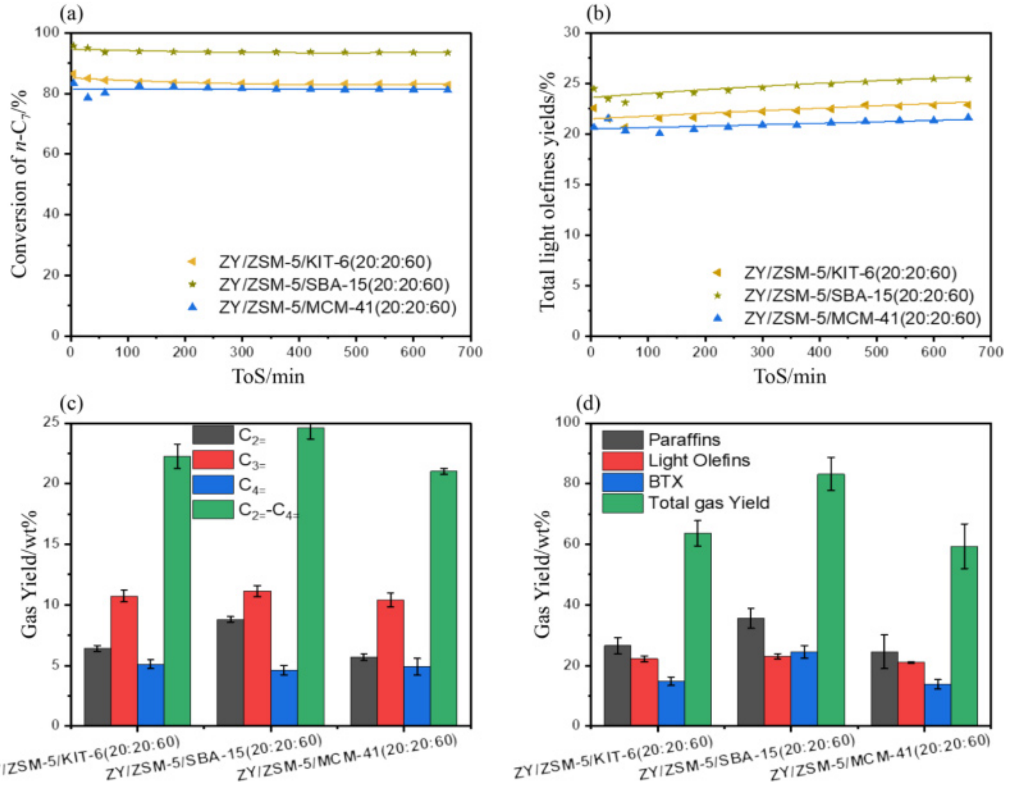

Fig. 6 Longevity tests of the selected composite catalysts at 550 °C and atmospheric pressure (ToS = 12 h and WHSV = 0.4 h^{-1}): (a) n-C_7 conversion; (b) total yield of LOs; (c) product distribution of LOs, and (d) distribution of gas yields.

catalyst showed the best ability to crack n-C_7 with the stable conversions at 95%, followed by ZY/ZSM-5/KIT-6 (20:20:60). Conversely, the ZY/ZSM-5/MCM-41 (20:20:60) composite catalyst showed the initial decrease in n-C_7 conversion from 82% (within the first hour of ToS) the stabilized at about 79%. The three catalysts show rather stable total yields of LOs (Fig. 6(b)). ZY/ZSM-5/SBA-15 (20:20:60) produced the highest LOs yield at about 25%, while ZY/ZSM-5/MCM-41 (20:20:60) only achieved the LOs yield of about 21%. Detailed product distribution is shown in Figs. 6(c) and 6(d), showing that the three composites are selective to propylene, and ZY/ZSM-5/SBA-15 (20:20:60) and ZY/ZSM-5/KIT-6 (20:20:60) are also capable of producing ethylene and the aromatic compounds benzene, toluene and xylene (BTX). Overall, The MCM-41 mesoporous silica is less effective in the formation of composite catalysts for catalytic cracking, possibly due to the relatively smaller pore size of MCM-41 compared to SAB-15 and KIT-6, being less capable of improving diffusion and accessibility to the zeolites.

TGA was conducted to investigate the coke deposition of the used ZY/ZSM-5/KIT-6 (20:20:60), ZY/ZSM-5/MCM-41 (20:20:60), and ZY/ZSM-5/SBA-15 (20:20:60) composite catalysts after the longevity tests. The TGA was divided into 4 stages for a total of 12 h on stream, as shown in Fig. 7. The first stage heated the catalyst under N_2 from room temperature up to 200 °C (at 10 $°C \cdot min^{-1}$) and held for 1 h to remove the absorbed moisture from the composites. The second step was from 200 °C to 400 °C and held at 400 °C for 1 h to ensure the decomposition of the light hydrocarbons of C_1–C_5, which may be that possibly exist in the composite. The third step was from 400 °C to 650 °C and held at 650 °C for 1 h to remove heavy hydrocarbons. The final stage performed at 650 °C isothermally under air for 1 h to burn the remaining carbon residue from the catalysts. The results show that the three used catalysts of ZY/ZSM-5/KIT-6 (20:20:60), ZY/ZSM-5/MCM-41 (20:20:60), and ZY/ZSM-5/SBA-15 (20:20:60) displayed weight losses of 0.4 wt %, 1.4 wt %, and 1.5 wt %, respectively, at the final stage, suggesting that they are relatively resistant to coking during the reaction.

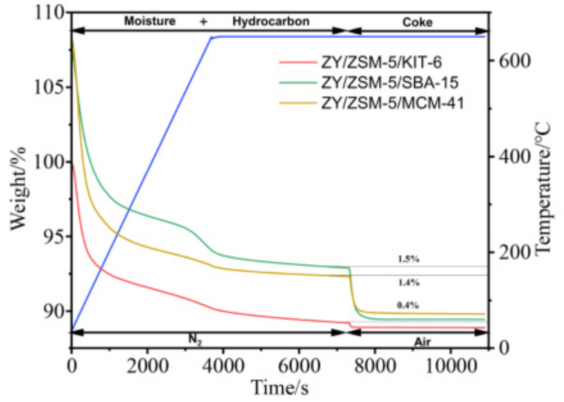

Fig. 7 TGA profiles of the used ZY/ZSM-5/KIT-6 (20:20:60), ZY/ZSM-5/SBA-15 (20:20:60), and ZY/ZSM-5/MCM-41 (20:20:60).

3.3 PFG-NMR study of self-diffusion of n-C_7 within the selected composite catalysts

To study the structure-diffusion-performance relationship of the selected composite catalysts, PFG-NMR characterization was conducted to investigate the diffusion of n-C_7 within the composites. We first performed the measurement using the neat n-C_7 at room temperature to estimate the self-diffusion coefficient (D_{self}). Figure S7 (cf. ESM) shows the log attenuation plot for the free bulk liquid n-C_7 sample, which is linear as expected, and the calculated D_{self} value for n-C_7 is 32.4×10^{-10} $m^2 \cdot s^{-1}$, being consistent with the reported value [33]. The $\log_{10}$ attenuation plots for the n-C_7 saturated composites are shown in Fig. 8, which are nonlinear attenuation curves, showing the distinct presence of two linear regions. The first region represents the self-diffusivity of n-C_7 (D_1) in the intercrystallite regimes of the composites, which could be influenced by the size and shape of the zeolite/silica particles, while the second indicate the self-diffusivity within the frameworks of the components, i.e., the intracrystalline diffusivity (D_2) [34].

The calculated values for D_1 and D_2 of the n-C_7 saturated composite catalysts are presented in Table 4. Comparatively, ZY/ZSM-5/KIT-6 (20:20:60) has the largest D_1 value of $11.2 \pm 0.2 \times 10^{-10}$ $m^2 \cdot s^{-1}$ among the three composites, followed by ZY/ZSM-5/SBA-6 (20:20:60) with $D_1 = 9.7 \pm 0.1 \times 10^{-10}$ $m^2 \cdot s^{-1}$, indicating that the effective diffusion of n-C_7 molecules through the intercrystallite region of the two composites. Conversely, the D_1 value of ZY/ZSM-5/MCM-41(20:20:60) is the lowest at $6.9 \pm 0.1 \times 10^{-10}$ $m^2 \cdot s^{-1}$, which corresponds to the conversion data (Fig. 6(a)), indicating that catalytic conversion of n-C_7 within the composites was affected by

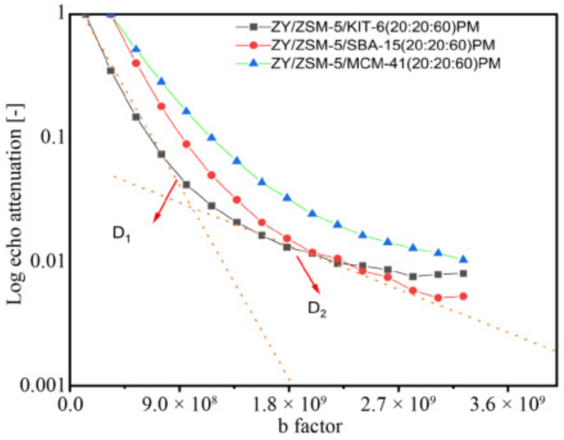

Fig. 8 Log_{10} attenuation plots of n-C_7 saturated composite catalysts under investigation.

Table 4 Relevant diffusion coefficients and calculated tortuosity values by PFG-NMR

Composite	D_{self} of n-C_7	D_1 (10^{-10} $m^2 \cdot s^{-1}$)	D_2	τ_1	τ_2
ZY/ZSM-5/KIT-6 (20:20:60)	32.4	11.2 ± 0.2	2.0 ± 0.2	2.9	16.3
ZY/ZSM-5/SBA-15 (20:20:60)		9.7 ± 0.1	2.4 ± 0.2	3.4	13.7
ZY/ZSM-5/MCM-41 (20:20:60)		6.9 ± 0.1	1.7 ± 0.1	4.7	19.3

the intercrystallite diffusion of reactant molecules.

Compared to the intercrystallite diffusivity (D_1), the intracrystalline diffusivity (D_2) was about half a magnitude lower, suggesting the higher diffusion resistance within the frameworks of zeolites/silicas than that in the space between their particles. Since the proportion of the three components of the composite catalysts was the same at 20 wt % for ZY, 20 wt % for ZSM-5, and 60 wt % for silica, then the D_2 values of the composites under investigation could be correlated to the averaged pore diameters of the mesoporous silicas employed. As shown above (Fig. S1), the pore diameters of the silica follow the order of SBA-15 > KIT-6 > MCM-41, corresponding well to the calculated D_2 values of $2.4 \pm 0.2 \times 10^{-10}$ $m^2 \cdot s^{-1} > 2.0 \pm 0.2 \times 10^{-10}$ $m^2 \cdot s^{-1} > 1.7 \pm 0.1 \times 10^{-10}$ $m^2 \cdot s^{-1}$.

The intercrystallite and intracrystalline tortuosity (τ_1 and τ_2) values are calculated by comparing the bulk self-diffusivity (D_{self}) to D_1 and D_2, as presented in Table 4, and a higher τ value suggests more restrictive diffusion within the considered domain [35,36]. The values of τ_2 are larger than that of τ_1, which is reasonable since intracrystalline diffusion resistance is higher than that of the intercrystallite diffusion due to the significantly reduced diffusion length scale within the framework materials. Table 4 shows that ZY/ZSM-5/SBA-15 (20:20: 60) has the smallest τ_2 value of 13.7 and moderate τ_1 value of 3.4.

Compared to the other two composites, ZY/ZSM-5/MCM-41 (20:20:60) has the highest τ value of 4.70, indicating the presence of a intercrystalline pore network with significant diffusion resistance. This is in line with its lower self-diffusion coefficient compared to ZY/ZSM-5/KIT-6 (20:20:60) and ZY/ZSM-5/SAB-15 (20:20:60), which have tortuosity of 2.89 and 3.35, respectively. Findings here suggest that by engineering the heterogeneous meso-microporosity, diffusion within a composite catalyst can be tuned to enhance the cracking performance.

4 Conclusions

In the study, the successfully synthesized of formulated catalysts was confirmed through detailed XRD and BET analyses. An XRD analysis confirmed the integrity of ZY and ZSM-5 frameworks within the composites. At the same time, BET results indicated that external surface areas and mesopore volumes had decreased by 10%–20%, while microporosity had increased by 50%–55%, suggesting a well-balanced micro-mesopore structure conducive to catalysis. Based on the results of the zeolite composites with different silica supports, pore size is an important factor in catalytic performance. Additionally, the PFG-NMR study indicates that the structure of composite catalysts influences n-C_7 self-diffusion. In the intercrystallite region, there is less resistance than in the intercrystalline regions, indicating higher intercrystallite diffusivity (D_1). The composite ZY/ZSM-5/KIT-6 (20:20:60) shows the highest diffusion coefficient. In the case of ZY/ZSM-5/MCM-41 (20:20:60), the tortuosity values indicate that intercrystalline diffusion faces greater resistance. In general, LO selectivity and conversion of n-C_7 are affected by the diffusion characteristics of catalysts, and meso-microporosity can be adjusted to optimize. Due to the narrower and smaller mesopores range in MCM-41, the composite ZY/ZSM-5/MCM-41 (20:20:60) converted 79% n-C_7. With larger mesopores in KIT-6, the ZY/ZSM-5/KIT-6 composite (20:20:60) achieved an 84% conversion rate. ZY/ZSM-5/MCM-41 (20:20:60) exhibited the lowest yield of LOs (21%), followed by ZY/ZSM-5/KIT-6 (20:20:60) (22%), and ZY/ZSM-5/SBA-15 (20:20:60) (24%), demonstrating the importance of mesoporous structures for diffusion and accessibility of reactants. Overall, this research suggests the potential of zeolite-mesoporous silica composite catalysts in catalysis and separation applications. It is possible to develop highly efficient and selective catalysts for industrial applications by combining microporous and mesoporous structures within these composites.

Competing interests The authors declare that they have no competing interests.

Acknowledgements H.A. thanks the financial support provided by the Ministry of High Education of Saudi Arabia for his PhD secondment at The University of Manchester. Z.Q. thanks the financial support of the China Scholarship Council for his PhD secondment at The University of Manchester (CSC file No. 201906120207). The authors also thank the UK Catalysis Hub for its resources and support.

Electronic Supplementary Material Supplementary material is available in the online version of this article at http://doi.org/10.1007/s11705-024-2480-7 and is accessible for authorized users.

References

1. Zhao S, Li H, Wang B, Yang X, Peng Y, Du H, Zhang Y, Han D, Li Z. Recent advances on syng as conversion targeting light olefins. Fuel, 2022, 321: 124124
2. Chernyak S, Corda M, Dath J, Ordomsky V, Khodakov A. Light olefin synthesis from a diversity of renewable and fossil feedstocks: state-of-the-art and outlook. Chemical Society Reviews, 2022, 51(18): 7994–8044
3. Tabibian S, Sharifzadeh M. Statistical and analytical investigation of methanol applications, production technologies, value-chain and economy with a special focus on renewable methanol. Renewable & Sustainable Energy Reviews, 2023, 179: 113281
4. De Graaf B, Fletcher R A Y. On-demand propylene from naphtha: preparing for change. www.digitalrefining.com. Accenture Website, 2023
5. Fattahi N, Triantafyllidis K, Luque R, Ramazani A. Zeolite-based catalysts: a valuable approach toward ester bond formation. Catalysts, 2019, 9(9): 758
6. Alabdullah M A, Shoinkhorova T, Dikhtiarenko A, Ould-Chikh S, Rodriguez-Gomez A, Chung S, Alahmadi A O, Hita I, Pairis S, Hazemann J, et al. Understanding catalyst deactivation during the direct cracking of crude oil. Catalysis Science & Technology, 2022, 12(18): 5657–5670
7. Al-Shammari A, Ali S, Al-Yassir N, Aitani A, Ogunronbi K, Al-Majnouni K, Al-Khattaf S. Catalytic cracking of heavy naphtha-range hydrocarbons over different zeolites structures. Fuel Processing Technology, 2014, 122: 12–22
8. Xian X, Ran C, Yang P, Chu Y, Zhao S, Dong L. Effect of the acidity of HZSM-5/MCM-41 hierarchical zeolite on its catalytic performance in supercritical catalytic cracking of *n*-dodecane: experiments and mechanism. Catalysis Science & Technology, 2018, 8(16): 4241–4256
9. Abdulridha S, Zhang R, Xu S, Tedstone A, Ou X, Gong J, Mao B, Frogley M, Bawn C, Zhou Z, et al. An efficient microwave-assisted chelation (MWAC) post-synthetic modification method to produce hierarchical Y zeolites. Microporous and Mesoporous Materials, 2021, 311: 110715
10. Jermy B, Siddiqui M, Aitani A, Saeed M, Al-Khattaf S. Utilization of ZSM-5/MCM-41 composite as FCC catalyst additive for enhancing propylene yield from VGO cracking. Journal of Porous Materials, 2012, 19(4): 499–509
11. Zhao D, Huo Q, Feng J, Chmelka B, Stucky G. Nonionic triblock and star diblock copolymer and oligomeric surfactant syntheses of highly ordered, hydrothermally stable, mesoporous silica structures. Journal of the American Chemical Society, 1998, 120(24): 6024–6036
12. Choi D, Ryoo R. Template synthesis of ordered mesoporous organic polymeric materials using hydrophobic silylated KIT-6 mesoporous silica. Journal of Materials Chemistry, 2010, 20(26): 5544–5550
13. Kleitz F, Choi S, Ryoo R. Cubic *Ia* 3*d* large mesoporous silica: synthesis and replication to platinum nanowires, carbon nanorods and carbon nanotubes. Chemical Communications, 2003, 17(17): 2136–2137
14. Forster L, Lutecki M, Fordsmand H, Yu L, D'Agostino C. Tailoring morphology of hierarchical catalysts for tuning pore diffusion behaviour: a rational guideline exploiting bench-top pulsed-field gradient (PFG) nuclear magnetic resonance (NMR). Molecular Systems Design & Engineering, 2020, 5(7): 1193–1204
15. La-Salvia N, Lovón-Quintana J, Lovón A, Valença G. Influence of aluminium addition in the framework of MCM-41 mesoporous molecular sieve synthesized by non-hydrothermal method in an alkali-free system. Materials Research, 2017, 20(6): 1461–1469
16. Abbaspour S, Nourbakhsh A, Kalbasi R, Mackenzie K. Investigating the properties of the nanocomposite (poly(4-vinyl pyridine)/Al-SBA-15): a precursor for β-SiAlON. Molecular Crystals and Liquid Crystals, 2012, 555(1): 104–111
17. Zhao D, Feng J, Huo Q, Melosh N, Fredrickson G, Chmelka B, Stucky G. Triblock copolymer syntheses of mesoporous silica with periodic 50 to 300 angstrom pores. Science, 1998, 279(5350): 548–552
18. Gaudin P, Dorge S, Nouali H, Kehrli D, Michelin L, Josien L, Fioux P, Vidal L, Soulard M, Vierling M, et al. Synthesis of Cu-Ce/KIT-6 materials for SO_x removal. Applied Catalysis A, General, 2015, 504: 110–118
19. Florek J, Guillet-Nicolas R, Kleitz F. Ordered mesoporous silica: synthesis and applications. Functional Materials for Energy, Sustainable Development and Biomedical Sciences, 2014, 61–100
20. Merkache R, Fechete I, Maamache M, Bernard M, Turek P, Al-Dalama K, Garin F. 3D ordered mesoporous Fe-KIT-6 catalysts for methylcyclohexane (MCP) conversion and carbon dioxide (CO_2) hydrogenation for energy and environmental applications. Applied Catalysis A, General, 2015, 504: 672–681
21. Beltrán-Osuna Á, Gómez Ribelles J, Perilla J. A study of some fundamental physicochemical variables on the morphology of mesoporous silica nanoparticles MCM-41 type. Journal of Nanoparticle Research, 2017, 19(12): 381
22. Gao Q, Zhang Y, Zhou K, Wu H, Guo J, Zhang L, Duan A, Zhao Z, Zhang F, Zhou Y. Synthesis of ZSM-5/KIT-6 with a tunable pore structure and its catalytic application in the hydrodesulfurization of dibenzothiophene and diesel oil. RSC Advances, 2018, 8(51): 28879–28890
23. Piciorus E, Svera P, Ianasi C. Porous silicas from mixtures of $Na_2Si_3O_7$ aqueous solution and teos. Influence of sodium silicate amount. Studia Universitatis Babes-Bolyai. Chemia, 2021, 66(1): 35–48
24. Keshavarz H, Khavandi A, Alamolhoda S, Naimi-Jamal M. pH-sensitive magnetite mesoporous silica nanocomposites for controlled drug delivery and hyperthermia. RSC Advances, 2020, 10(64): 39008–39016
25. Seddigi Z. Nature of the FTIR band in acidic zeolites. Reaction Kinetics and Catalysis Letters, 2001, 73(1): 63–70

26. Byrappa K, Kumar B. Characterization of zeolites by infrared spectroscopy. Asian Journal of Chemistry, 2007, 19(6): 4933–4935
27. Zhang R, Raja D, Zhang Y, Yan Y, Garforth A, Jiao Y, Fan X. Sequential Microwave-assisted dealumination and hydrothermal alkaline treatments of Y zeolite for preparing hierarchical mesoporous zeolite catalysts. Topics in Catalysis, 2020, 63: 340–350
28. Kouser S, Hezam A, Khadri M, Khanum S. A review on zeolite imidazole frameworks: synthesis, properties, and applications. Journal of Porous Materials, 2022, 29: 663–681
29. Zang J, Yu H, Liu G, Hong M, Liu J, Chen T. Research progress on modifications of zeolite Y for improved catalytic properties. Inorganics, 2023, 11(1): 22
30. Bukhtiyarova M, Echevskii G. Coke formation on zeolites Y and their deactivation model. Petroleum Chemistry, 2020, 60(4): 532–539
31. Daniel S, Monguen C, El Kasmi A, Arshad M, Tian Z. Oxidative dehydrogenation of propane to olefins promoted by Zr-modified ZSM-5. Catalysis Letters, 2023, 153(1): 285–299
32. Hou X, Zhao L, Diao Z. Roles of alkenes and coke formation in the deactivation of ZSM-5 zeolites during *n*-pentane catalytic cracking. Catalysis Letters, 2020, 150(9): 2716–2725
33. Forman E, Trujillo M, Ziegler K J, Bradley S, Wang H, Prabhakar S, Vasenkov S. Self-diffusion of heptane inside aggregates of porous alumina particles by pulsed field gradient NMR. Microporous and Mesoporous Materials, 2016, 229: 117–123
34. Kärger J. Measurement of diffusion in zeolites—a never ending challenge? Adsorption, 2003, 9(1): 29–35
35. D’Agostino C, Brett G, Miedziak P, Knight D, Hutchings G, Gladden L, Mantle M. Understanding the solvent effect on the catalytic oxidation of 1,4-butanediol in methanol over Au/TiO_2 catalyst: NMR diffusion and relaxation studies. Chemistry, 2012, 18(45): 14426–14433
36. Run Z, Xiao D, Yilai J, D’Agostino C, Wenfu Y, Fan X. Controllable synthesis, diffusion study and catalysis of hierarchical zeolites. Chemical Journal of Chinese Universities, 2021, 42(1): 74–100